Investigating the Impact of Pores on Rock Damage during Thermal Spalling Drilling

Weiji Liu [iD][1,2,3,*], Feilong Yang[1] and Xiaohua Zhu [iD][1,2,3]

[1]*School of Mechatronic Engineering, Southwest Petroleum University, Chengdu 610500, China*
[2]*Oil and Gas Equipment Technology Sharing and Service Platform of Sichuan Province, Chengdu 610500, China*
[3]*Geothermal Energy Research Center, Southwest Petroleum University, Chengdu 610500, China*

ARTICLE INFO

ABSTRACT

Numerous microcracks and pores in geological rock formations cause early flaws. High temperatures increase these fractures and pores, thermally damaging reservoir rocks and changing the rock failure mechanism. However, research on pores' high-temperature thermal spalling and fragmentation effects on heterogeneous rocks is sparse. This study built a finite element numerical model of heterogeneous granite rock thermal damage with pores based on rock thermal fracture theory and the Voronoi method and explored the mechanism under varied pore settings. The research's findings indicate that the application of high temperatures to local heterogeneous porous rocks results in a higher proportion of tensile damage. The proportion of shear damage and tensile damage constantly varies due to the changing position and shape of the pores. The rock's porosity has the effect of decreasing temperature in the direction of heat transfer while increasing the extent of temperature transfer along the pore parallel to the heating surface. The potential degree of damage increases as the density of pores increases, the distances between them decrease, and the pore lengths increase. The thermal damage resulting from heating in the vicinity of the pore is primarily localized in the area between the pore and the heated surface. This effect becomes more significant as the distance between them decreases. The findings of this study can serve as a theoretical framework for understanding the impact of rock pores on rock thermal fracturing and fragmentation in the thermal spalling-assisted development of deep oil and gas resources.

*Corresponding Authors
Email: lwj2017_swpu@163.com
Tel: +(86) 13688465071

1. Introduction

With the rapid development of modern industry, the demand for oil and gas resources has greatly increased, and the exploration and development of oil and gas resources has gradually shifted from shallow strata to deep hard strata [1-9]. Traditional mechanical drilling techniques rely on the shearing action of the drill bit to achieve the purpose of crushing rocks. This leads to severe wear on the drill bit, and the mechanical drilling speed is low, making it difficult to control drilling costs [10-16]. Thermal spalling drilling technology is a non-contact and efficient rock-breaking technology, suitable for drilling into hard strata, and has been widely used [17-22]. However, there is little research on the impact of high-temperature flames on the initial pore of the rock, which can lead to changes in the rock-breaking mechanism in thermal spalling drilling. Therefore, conducting research on high-temperature heating of porous rocks and exploring the influence of pores on the law of thermal spalling rock breaking has a very positive effect on improving the development efficiency of thermal spalling drilling technology.

Large amounts of geometrically irregular and multiscale pores are widely and randomly distributed in rocks, mainly classified as connected pores, blind pores, capillary pores, and isolated pores [23-25]. Pore structure affects the occurrence of oil and gas resources and determines the permeability of reservoirs in matrix and fractures [26, 27]. Therefore, pore structure characterization and numerical model establishment are of great significance in predicting rock properties and reservoir classification and evaluation [28, 29]. By using techniques such as electron microscopy and CT scanning to study the connectivity of pore and fracture networks and estimate micro-porosity [30, 31], and then combining direct modeling methods, non-reconstructive model methods, and reconstructive model methods, numerical modeling of pore structures can be achieved [32]. The evolution law of the micro-pore structure of granite under a geothermal environment or high-temperature treatment can establish many relationships between macroscopic and microscopic characteristics [12]. Analysis of the morphological characteristics of granite pore structure and mineral particles at different temperatures shows that the porosity of granite increases as the temperature rises due to physical and chemical reactions [33]. Observation of the characteristics of the pore structure of heat-treated granite by using a micro-CT test system displays that thermal spalling is more likely to occur at the cement and crystal interface [34]. Using mercury intrusion porosity measurement method, the microstructural parameters of thermally treated granite in the temperature range of 25 to 1200°C were obtained, and it was found that the porosity of granite increased rapidly with increasing temperature, while the fractal dimension of pores showed a decreasing trend [35]. Identifying and quantifying the characterization parameters of connected pore rate and overall damage in thermal spall rocks of granite and evaluating their transport characteristics and mechanical strength respectively, it was found that porosity measurement only reflects the open porosity on the surface of rocks, while permeability measurement reflects the connected porosity [36]. At different temperatures, the porosity and permeability of rocks change significantly, and pores of different sizes exhibit different characteristics when heated. When conducting thermo-mechanical coupling analysis of granite, it was found that the trend of the micro-physical parameter values of super-micropores is completely opposite to that of mesopores and macro-pores [37-39], the fractal characteristics of mesopores and macro-pores are significant, and the fractal characteristics of micropores are the opposite. High temperature has a dual effect on the mechanical properties of rocks, and the fractal dimension of cross-scale pores is closely related to the mechanical properties of rocks [40]. Both the formation pressure gradient and the pseudocritical pressure gradient will decrease with the increase of total porosity and large pore porosity, and the nonlinear index (n) can be described by an exponential function with three parameters as the total porosity and large pore porosity change [41]. The heterogeneity of the mechanical and mineralogical properties of the mineral combination in porous rocks will produce local tensile stress when subjected to external loads, which will extend and expand in one direction along larger scales of pores, eventually forming rock fractures. Therefore, the method of using the multi-morphology extended pore and fracture coexistence theory to describe the interaction between pores and multi-morphology fractures in the medium has been widely used in the inversion of rock pore structures [42, 43].

Current research on rock pores mainly focuses on the evolution law of pores and changes in porosity and permeability at different temperatures. However, there is still a lack of research on the impact of rock porosity on the mechanism of rock breaking in thermal-spalling rocks. Therefore, this paper focuses on the heterogeneity of rock grain size, mineral content, and particle size to establish a numerical model of porous heterogeneous granite

thermal spalling damage. The effects of pore distance, pore length, and pore number on rock thermal spalling damage were studied. By revealing the influence of rock pore structure on the mechanism of thermal spalling, this paper provides a theoretical reference for the efficient development of deep oil and gas resources and the application of thermal spalling-assisted drilling technology.

2. Theoretical Backgrounds

2.1. Theory of Thermal Fracturing of Rock

2.1.1. Thermal Conduction of Rock

When heating rocks, heat is transferred from the high-temperature central zone to the low-temperature periphery (Fig. **1**). If two parallel and equally sized sections S are taken from the rock along the path of thermal conduction, with a temperature difference of ΔT between the two sections, a distance of Δn, and after a time dt, the amount of conducted heat can be expressed as:
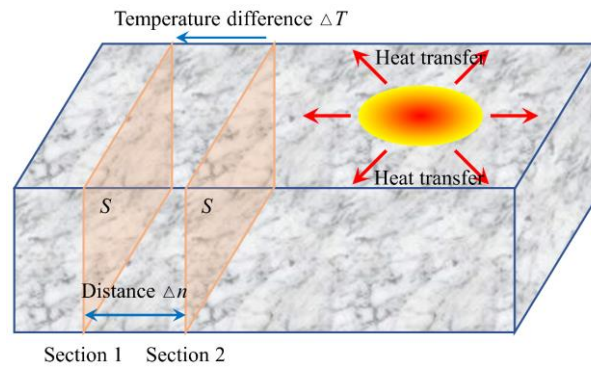

Figure 1: Schematic diagram of temperature transfer.

$$dQ = -\lambda \frac{\Delta T}{\Delta n} S dt \tag{1}$$

where, λ is the thermal conductivity coefficient, W/(m·K).

If we remove time and cross-sectional area from the above Eq. (1), we can obtain the calculation formula of the amount of heat q transmitted per unit time per unit area,

$$q = -\lambda \, grad T \tag{2}$$

Moreover, the temperature variation within the rock follows the heat conduction equation,

$$\frac{\partial T}{\partial t} = k \nabla^2 T \tag{3}$$

where, T is the temperature, K; t is the time, s; K is the thermal diffusivity coefficient, $K = \frac{\lambda}{\rho_m} - 1$, c is the specific heat of the rock, ρ_m is the density of the rock; ∇^2 is the Laplace operator, $\nabla^2 = \frac{\partial^2}{\partial x^2} + \frac{\partial^2}{\partial y^2} + \frac{\partial^2}{\partial z^2}$.

If the radius of the heat source is a and the time is t, then the general solution for the temperature of the rock at a point r from the origin is given by

$$T(r,t) = T_0 + (T_s - T_0) exp\left(-\frac{r^2 + a^2}{4kt}\right) \left\{ 1 - \sum_{k=0}^{\infty} \left(\frac{a}{r}\right)^k I_k\left(\frac{ar}{2kt}\right) \right\} \tag{4}$$

where, T_0 is the initial temperature of the rock; T_s is the temperature of the heat source; and I_k is the Modified Bessel Function of the First Kind.

2.1.2. The Thermal Stress Inside the Rock

Due to the short heating time of the rock and the large temperature gradient, rapid stress changes occur inside the rock, which is similar to thermal shock. After calculating the temperature at different points of the rock using the above Eq. (4), the formula for calculating the tensile stress caused by the thermal shock on the free surface of a semi-infinite body is used,

$$\sigma = B_i E\alpha \left(\rho_m c \right)^{\frac{1}{2}} \left(T \right) / \left(\lambda \right)^{\frac{1}{2}} \tag{5}$$

where, B_i is the Biot number (a dimensionless heat release coefficient), $B_i = \delta\gamma / \lambda$; α is the coefficient of linear thermal expansion of rocks; δ is the thickness of the rock that is being heated; γ is the heat emission coefficient.

The average tensile stress of granite at different temperatures can be calculated by Eq. (5). When the tensile stress exceeds the tensile strength of the rock, the rock undergoes tensile failure.

The rock will undergo thermal fragmentation when the shear stress generated by two adjacent isothermal surfaces exceeds the maximum shear stress of the rock,

$$\tau_T = \frac{\delta'}{\sqrt{k}} \cdot \frac{G}{S_P} \tag{6}$$

Where, δ′ is the coefficient of volumetric thermal expansion; G is the shear modulus; k is the thermal conductivity; s is the thermal fragmentation coefficient, and for granite, s=9.5.

2.2. The Constitutive Theory of Rock Damage

2.2.1. The Governing Equations of the Damage Field

Granite contains many primary cracks and the distribution of cracks and other defects is random. Therefore, when constructing a statistical damage model for rocks, it is considered that the strength of the microelement inside the rock follows the Weibull distribution [44], and its probability density function is given by:

$$P = \frac{m}{\varepsilon_0} \left(\frac{\varepsilon}{\varepsilon_0} \right)^{m-1} \exp\left[-\left(\frac{\varepsilon}{\varepsilon_0} \right)^m \right] \tag{7}$$

where, ε is the axial strain of the specimen, and ε_0 and m are parameters of the Weibull distribution. During dynamic loading, as the load increases, microelements inside the specimen gradually fail and lose their bearing capacity. According to the viewpoint of damage mechanics, the damage variable of the granite specimen under load is given by:

$$D_1 = \frac{n}{N} = \frac{\int_0^\varepsilon NP(\varepsilon)d\varepsilon}{N} = 1 - \exp\left[-\left(\frac{\varepsilon}{\varepsilon_0} \right)^m \right] \tag{8}$$

where, D_1 is the damage variable of the granite specimen under load; n is the number of failed microelements inside the specimen; N is the total number of microelements inside the specimen.

High temperature and water cooling treatment can cause initial damage to the granite specimen, resulting in the deterioration of its mechanical properties [45]. The initial damage variable of the granite specimen caused by high temperature and water cooling treatment can be expressed as,

$$D_T = 1 - \frac{E_T}{E_0} \tag{9}$$

where, T is the temperature of heat treatment; E_T is the elastic modulus of the granite after being subjected to high temperature and water quenching treatment; E_0 is the elastic modulus of the granite specimen at room temperature.

Therefore, the cumulative damage variable of the granite, which takes into account the damage under loading and that induced by high temperature-water quenching treatment, is given by,

$$D = 1 - (1 - D_1)(1 - D_T) = D_T + D_1 - D_1 D_T \tag{10}$$

The constitutive relationship of the granite after being subjected to high temperature-water quenching treatment under uniaxial dynamic loading is given by,

$$\sigma = (1 - D)E_0\varepsilon = (1 - D_1)(1 - D_T)E_0\varepsilon \tag{11}$$

In addition, considering the strain rate effect when the granite specimen after high temperature-water quenching treatment is subjected to dynamic loading, it can be obtained that,

$$\sigma = \eta(T)\dot{\varepsilon} \tag{12}$$

where, $\eta(T)$ is the viscosity coefficient of granite at a heat treatment temperature of T; $\dot{\varepsilon}$ is the strain rate of granite.

Therefore, taking into account the effects of load-induced damage, thermal treatment damage, and strain rate, the dynamic constitutive model for the high temperature-water quenched granite can be obtained as,

$$\sigma = (1 - D)E_0\varepsilon = (1 - D_1)(1 - D_T)E_0\varepsilon + \eta(T)\dot{\varepsilon} \tag{13}$$

Substituting Eq. (10) and Eq. (11) into Eq. (13), it can be obtained that,

$$\sigma = E_0\varepsilon - E_0\varepsilon \left\{ D_T + (1 - D_T)\left[1 - e^{-\left(\frac{\varepsilon}{\varepsilon_0}\right)^m} \right] \right\} + \eta(T)\dot{\varepsilon} \tag{14}$$

Although it has been found through experiments that this damage constitutive model is well-fitted to experimental curves, its applicability is limited for different rocks. In order to facilitate the study of rock damage, a damage variable is introduced into the multi-field coupling analysis equation [46, 47].
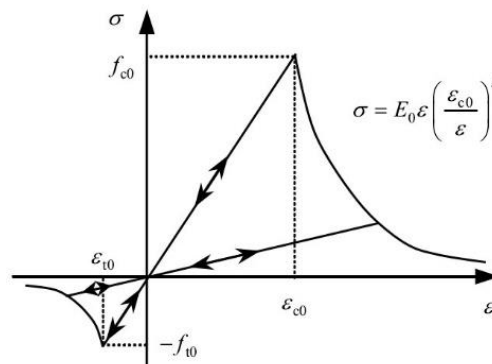

Figure 2: Constitutive relationship of rock under uniaxial stress state [47].

As can be seen from Fig. (**2**), when the compressive stress (strain) is positive, the porous medium is elastic at the initial stage of stress. According to the generalized Hooke's law, the porous medium satisfies the constitutive equation expressed by displacement, pore fluid pressure p (shrinkage is negative), and temperature change T as follows,

$$Gu_{i,jj} + \frac{G}{1-2v}u_{i,jj} + \alpha p_{,i} + K'\alpha_T T_{,i} + F_i = 0 \tag{15}$$

where, G is the shear modulus of the medium; v is the drained Poisson's ratio of the medium; α_T is the coefficient of thermal expansion of the medium under constant pore pressure conditions, $°C^{-1}$; α is the Biot's coefficient; F_i is the physical strength; u_i (i =x, y, z) is the displacement component in the direction i;

The drained bulk modulus of the medium is $K' = 2G(1+v)/3(1-2v)$.

The Biot's coefficient depends on the compressibility of the components in the medium and can be expressed as [48],

$$\alpha = 1 - \frac{K'}{K_s} = \frac{3(v_u - v)}{B(1-2v)(1+v_u)} \tag{16}$$

where, K_s is the effective bulk modulus of the solid components; B is the Skempton coefficient; v_u is the drained Poisson's ratio of the solid components.

Using the compressive strength, tensile strength, thermal stresses, and thermal strains of rock, the concept of thermal damage of rock can be defined. Firstly, stress state functions F1 and F2 are introduced, which respectively represent the tensile damage and shear damage occurring when the stress state of the medium satisfies the maximum tensile stress criterion and the Mohr-Coulomb criterion,

$$F_1 = -\sigma_3 - f_{t0} \tag{17}$$

$$F_2 = -\sigma_1 - \sigma_3 \frac{1+\sin\phi}{1-\sin\phi} - f_{c0} \tag{18}$$

where, f_{t0} is the elastic limit tensile stress of rock; f_{c0} is the elastic limit compressive stress of rock; σ_1 is the first principal stress; σ_3 is the third principal stress; ϕ is the angle of friction for rock.

When F_1 and F_2 are greater than or equal to zero, rock undergoes tension damage and shear damage. It should be noted that under any stress conditions, tension damage is prioritized.

The damage variable of rock is represented as [49, 50],

$$D = \begin{cases} 0 & F_1 < 0 \text{、} F_2 < 0 \\ 1 - \left| \dfrac{\varepsilon_{t0}}{\varepsilon_3} \right|^n & F_1 \geq 0 \text{、} dF_1 > 0 \\ 1 - \left| \dfrac{\varepsilon_{c0}}{\varepsilon_1} \right|^n & F_2 \geq 0 \text{、} dF_2 > 0 \end{cases} \tag{19}$$

where, ε_{t0} is the maximum tensile principal strain of the element when the rock undergoes tensile damage; ε_{c0} is the maximum compressive principal strain of the element when the rock undergoes shear damage; ε_1 is the first principal strain; ε_3 is the third principal strain; n is a coefficient used for the element damage evolution, and here we set n=2.

$dF_1 > 0$ and $dF_2 > 0$ respectively represent the continued loading states after two different types of damage, which can result in the accumulation of damage parameters. $dF_1 < 0$ and $dF_2 < 0$, on the other hand, indicate unloading states where there is no new damage accumulation, and the damage parameters remain the same as the previous loading or time step.

2.2.2. The Effect of Damage on Various Physical Field Parameters

Based on the theory of elastic damage, the elastic modulus of the element after damage can be expressed as:

$$E = (1 - D) E_0 \tag{20}$$

where, E_0 is the elastic modulus before damage; E is the elastic modulus after damage.

It is assumed here that the damage and its evolution are isotropic, so E_0, E and D are all scalars. Damage must necessarily cause an increase in the rock's conductive coefficient. As a preliminary study, the effect of damage on the thermal conductivity coefficient is expressed as [51],

$$\lambda_s(T, D) = \lambda_s(T) \exp(D / \alpha_\lambda) \tag{21}$$

where, α_λ is the coefficient of the effect of damage on thermal conductivity.

The porosity of rock formations is related to the stress state they are subjected to, and this relationship can be expressed as,

$$\phi = (\phi_0 - \phi_r) \exp(-\alpha_\phi \overline{\alpha}_v) + \phi_r \tag{22}$$

where, ϕ_0 is the porosity when under stress; α_ϕ is the the stress sensitivity coefficient of porosity, which can be taken as $5.0 \times 10^{-8} Pa^{-1}$; ϕ_r is the limit value of porosity under high compressive stress; $\overline{\alpha}_v$ is the mean effective stress, which can be calculated using the following equation:

$$\overline{\alpha}_v = (\sigma_1 + \sigma_2 + \sigma_3) / 3 - \alpha p \tag{23}$$

where, α is the Biot coefficient, which can be calculated according to Eq. (16). σ_1、 σ_2 and σ_3 are three principal stresses. In addition, the relationship between permeability and porosity can be assumed to follow the following power law function:

$$k = k_0 (\phi / \phi_0)^3 \tag{24}$$

When rocks are damaged, the evolution of their porosity and permeability becomes quite complex. Here, the following equation is used to reflect the effect of damage on porosity:

$$k = k_0 (\phi / \phi_0)^3 \exp(\alpha_k D) \tag{25}$$

where, α_k is the coefficient of damage effect on permeability, and its value is set to α_k=5.0.

2.3. Description of Granite Heterogeneity

The grain size and volume fraction of different minerals are different, and the average grain size Ra of the numerical model is expressed as [52],

$$R_a = \sum_{i=1}^m \omega_i r_i \tag{26}$$

where, ω_i is the volume fraction of different composition minerals; r_i is the average particle size of different composition minerals, mm; m is the number of mineral species.

The definition of the dimensionless heterogeneity index H is,

$$H = \sqrt{\sum_{i=1}^{m}\left(\frac{r_i}{R_a}-1\right)^2} \tag{27}$$

2.4. Control of Rock Porosity

When establishing porosity in COMSOL Multiphysics 5.6, different mathematical distributions are utilized to define the size, direction, and pore size distribution of rock pores. Examples of these distributions include random, power-law, Fisher, and size ratio distributions. The definition formulas for each distribution are as follows,

Random distribution: the probability density function of variable x follows a random distribution as follows,

$$f(x) = \begin{cases} \dfrac{1}{x_{max}-x_{min}} & x_{min} \leq x \leq x_{min} \\ 0 & else \end{cases} \tag{28}$$

Power-law distribution: the probability density function of variable x follows a power-law distribution as follows,

$$f(x) = \frac{\alpha-1}{x_{min}}(\frac{x}{x_{min}})^{-\alpha} \tag{29}$$

Fisher distribution: the probability density function of the Fisher distribution describes the mean angle (SI units: rad) of the angular deviation θ relative to the direction of the ellipse,

$$f(x) = K\frac{\sin\theta_e^{K\cos\theta}}{e^K-e^{-K}} \tag{30}$$

where, K is the dispersion coefficient or Fisher constant.

Size ratio distribution: the aperture a (SI units: meters) is directly proportional to the length of the fracture l,

$$a = cl \tag{31}$$

where, c is the proportionality factor.

3. Numerical Model of Porosity in Heterogeneous Rock

3.1. Establishment of Porosity Model in Heterogeneous Rock

The heterogeneity of rocks is simulated by the modeling method of Voronoi polyhedron with specified average particle size and different volume fractions, and the control method of heterogeneity is displayed in Eq. (27). Firstly, crystal parameters are selected according to the predetermined heterogeneity. To make the crystal parameters reasonable, the heterogeneous rock samples used in this study are granite from Suizhou, Hubei. The mineral content and material properties of the granite were determined by laboratory experiments, and the rock mineral content and grain size are manifested in Table **1**. Using PFC to group particles according to volume fraction, Voronoi polyhedra are generated and the grouping information is assigned to the Voronoi polyhedra before dividing the mesh. Then, different component material parameters of the rock are added according to different groups, and finally, the data of each mesh node is extracted and imported into COMSOL Multiphysics 5.6 to generate the material model of heterogeneous rock [53]. By calibrating the material properties of granite, the micro-material parameters of granite are obtained as revealed in Table **2** [54].

Table 1:   Basic mineral distribution of granite.

Mineral Types	Muscovite	Quartz	Albite	Microcline	Chlorite
Particle Size Range (MM)	1~1.8	2~3	3~4	1.2~2	1~2
Mineral Content (%)	7.8	12.2	34.5	41.1	4.4

Table 2:   Material properties of initial heterogeneous granite.

Material Properties/Grain Type	Albite	Quartz	Chlorite	Muscovite	Microcline	Boundary
Density (kg/m^3)	2540	2630	2600	2800	2630	2200
Specific heat capacity (J/(kg·k))	711	750	820	760	711	870
Coefficient of thermal expansion (1/K)	$1.067×10^{-5}$	$1.6×10^{-5}$	$0.75×10^{-5}$	$1.21×10^{-5}$	$0.75×10^{-5}$	$0.5×10^{-5}$
Thermal conductivity (W/(m·K))	3.26	4.94	3.26	3.14	2.34	5.0
Porosity	0.16	0.009	0.018	0.009	0.009	0.05
Young's modulus (GPa)	55	75	49	32	53	22
Poisson's ration	0.12	0.08	0.14	0.16	0.13	0.168

Based on the material model of heterogeneous granite, a porosity model of heterogeneous rocks is established (Fig. **3**), and the generation methods of different pores are defined using the development tools of COMSOL Multiphysics 5.6. The pore generation methods are controlled by the rock pore control theory in section 2.4, and the method is called in the global definition to generate irregular pore structures with different numbers, sizes, and positions to simulate the irregular pore structure in the real rock mass. In addition to the material of the heterogeneous rock matrix, the material inside the pore is a special rock structure in the real rock mass, and the pore is filled with air medium. The material parameters for the application in COMSOL Multiphysics 5.6 are exhibited in Table **3**.
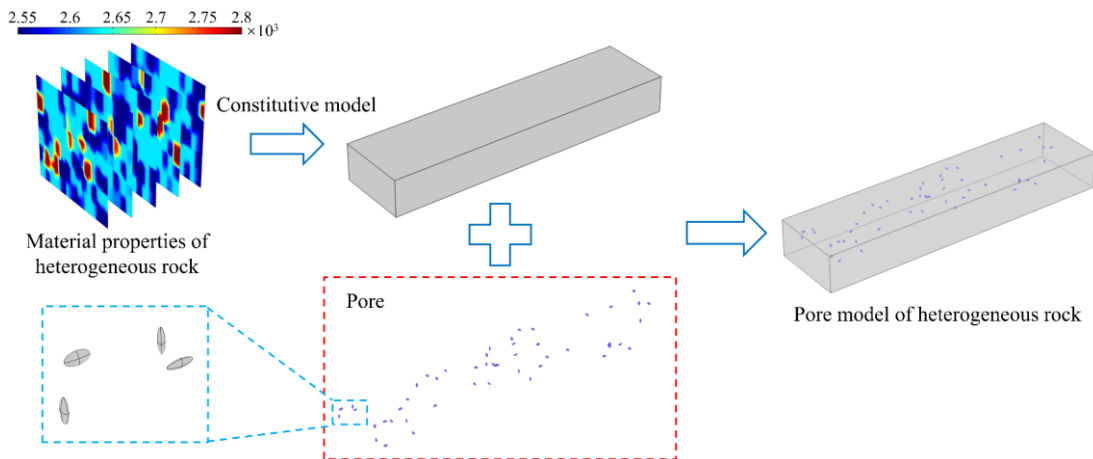
Figure 3: Porosity model of heterogeneous rock.

Table 3:   Material parameters of air.

Density	Heat Capacity at Constant Pressure	Thermal Conductivity
1.28kg/m³	1004J/(kg·K)	0.023W/(m·K)

3.2. Numerical Experiment Scheme

A computational model with multiple pores was established, where ellipsoids were used to simulate random pores for 3D pores. The size and shape controlling parameters for random pores include the lengths of three orthogonal a, b, and c semi-axes. The parameters controlling the position of pores include x, y, z coordinates and the rotation angle parameters for pores. COMSOL Multiphysics 5.6 includes various rotation axis types, such as x-axis rotation angle, y-axis rotation angle, z-axis rotation angle, Cartesian rotation coordinates, and spherical rotation parameters.

To accurately describe and analyze the different directions of ellipsoids in 3D space, the following definitions were made for the three orthogonal sections of the ellipsoid: the largest section of the ellipsoid is the section α; the smallest section is the section γ; and the section perpendicular to both the section α and the section γ is the section β, as announced in Fig. (**4**).
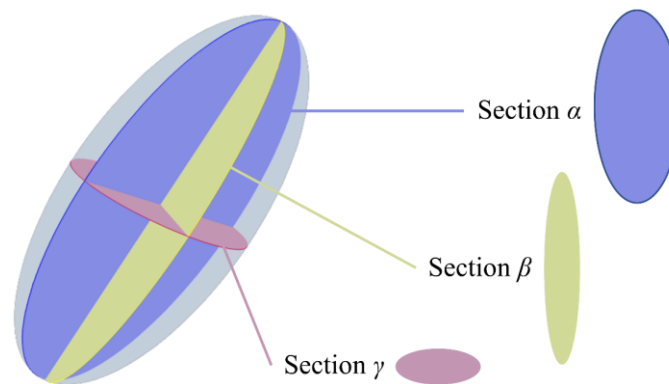

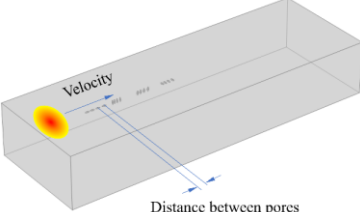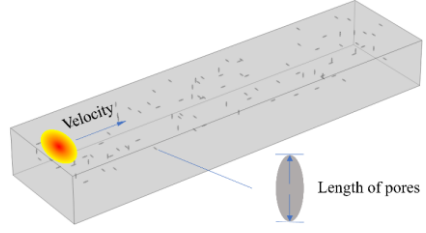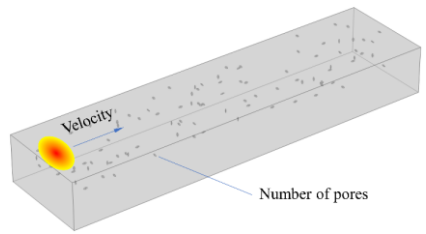**Figure 4:** Three orthogonal sections of an ellipsoid in 3D.

To study the effects of pore spacing on the heating of rocks, pores of the same size were generated and arranged along three semi-axis directions in the heating direction with gap distances of 0.2mm, 0.3mm, and 0.4mm, respectively. Based on the above pore arrangement, the heat source moving speed was changed to 5cm/s, 10cm/s, 15cm/s, and 20cm/s, respectively, with a fixed heating radius of R=7mm to study the effect of different heating depths on the interference between pores. The granite can be heated to a temperature of 700–1200°C using 500W of heating power, which is by actual geological circumstances. Additionally, to study the effect of different pore lengths on the thermal damage behavior of rocks, pore models with 100 pores of 5 different sizes were established, where the lengths of two semi-axes were equal to 0.1mm, and the length of the third semi-axis was changed to 0.1mm, 0.2mm, 0.3mm, 0.4mm, and 0.5mm, respectively. The effect of pore density on rock thermal damage was also considered, and heating was carried out under the conditions of v=5cm/s and R=7mm for each pore model. Random position distribution functions were established for 25, 50, 75, and 100 random positions in the refined rectangular parallelepiped, respectively. As real rock pores are very small, and there is currently no software available for studying nanoscale pores, the pore models established in this study were reduced in size as much as possible within the computational range. The lengths of the three semi-axes controlling the size and shape parameters of the pores were randomly chosen to be 0.1mm, 0.2mm, and 0.5mm, and the rotation angles around the x, y, and z axes were also randomly chosen within a specified range, and the pores were generated randomly within the specified range. The numbers and schematic diagrams of the rocks with pores are unveiled in Table **4**.

4. Simulation Results and Analysis

4.1. Pore Stress

For a random single pore, the stress and damage of different sections of the pore under different temperatures vary. To analyze the damage mechanism of cracks in the pore under heating conditions, temperature, and

Table 4: Computational models of heterogeneous porous rock.

Pore Number	Velocity (cm/s)	
K1	5	
K2	10	
K3	15	
K4	20	
	Length of pores (mm)	
K5	0.1	
K6	0.2	
K7	0.3	
K8	0.4	
K9	0.5	
	Number of pores	
K10	25	
K11	50	
K12	75	
K13	100	

stress analyses were carried out on different positions and sections of the random pore. Fig. (**5**) exhibits the temperature, stress, and damage of different sections of the random pore. From the temperature of the section α of the pore, it can be seen that the heat source is transmitted from the upper right to the lower left. When passing through the pore, the temperature of the bottom of the pore along the direction of heat transfer is slightly reduced. Therefore, it can be found from the corresponding damage distribution that the damage near the pore position along the direction of temperature transfer has a more significant increase, while the damage at the end of the long axis is relatively small. It can be seen that the heat source heating path of section β is from left to right on the upper surface, and the overall temperature distribution is transmitted from top to bottom. There is a significant difference in the stress distribution of the two pores in Fig. (**5**). The stress distribution of pore 1 is similar to that of the pore in section α, and the stress is higher at the short axis of the ellipse. In contrast, the point of higher stress in pore 2 appears at the top end of the long axis, and the short axis of the ellipse has higher stress. The damage distribution of pore 1 is similar to the stress distribution, while there is a sudden change in damage at the left end of the long axis of pore 2. The temperature distribution of the section γ pore is similar to that of the section α pore, but the temperature gradient is greater. The long axis direction of the section forms an acute angle with the direction of heat transfer and is not in coincidence or perpendicular to it. Therefore, the stress distribution is affected by both the direction of temperature transfer and the long-axis direction. The stress at the two vertices of the long axis is directed towards two different directions, and the stress in the short axis direction is also slightly different. The damage distribution of the rock spreads from the heat source center to the high-temperature end of the long axis.

Comparing the temperature distribution of different sections, it is found that the temperature will be weakened when passing through the pore, and the elliptical end far from the heat source center has a lower temperature, while the rock has a relatively uniform heat transfer. Different heating environments cause the pores to exhibit different stress characteristics, and the temperature change when passing through the pores will cause a sudden change in thermal stress. From the stress distribution, it can be seen that the stress at the nearest and farthest ends along the heat transfer path is small (for example, the stress value at the upper and lower endpoints of the section α), while the stress at the two endpoints perpendicular to the heat transfer path is high (for example, the stress value at the left and right endpoints of the section α). This is because the higher temperature end is

thermally expanded, and its surface is an upward protruding arc, similar to an "arch structure". The stress will be transmitted to both ends of the arc, resulting in the phenomenon of high stress at both ends or low stress at both ends. The damage and stress distribution of the rock can correspond to each other. When the stress reaches the damage threshold, damage occurs, and the greater the stress, the greater the damage value. The stress and damage are not related to the direction of each axis of the pore but are related to the location of the pore and the section it is on concerning the direction of heat transfer.
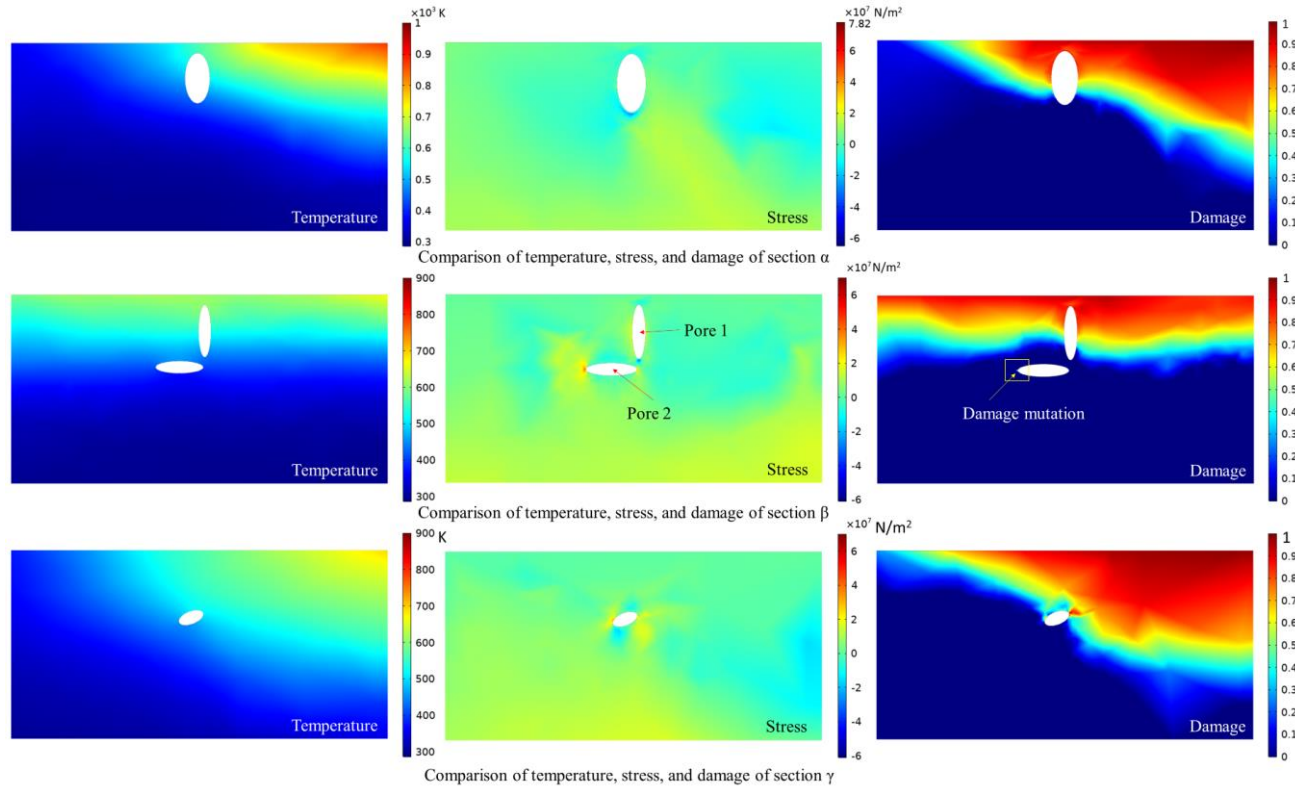

Figure 5: Comparison of temperature, stress, and damage at different cross-sections of random pores.

It can be concluded that during the heat transfer process, ellipsoidal three-dimensional pores will cause a temperature decrease along the heat transfer direction because the thermal conductivity of the pore is lower than that of the rock. Compared with other parts of the rock, the pore has a greater temperature gradient, which leads to an increase in thermal stress in the rock. In addition, there is a significant correlation between the stress of the pore and the isothermal surface. When the pore is spread along the isothermal surface, the stress value is similar. When comparing the elliptical stress distribution of different sections, since the curvature at the long axis of the pore cross-section is higher, the stress concentration is more obvious, so the end of the pore is more prone to stress concentration and damage under the same temperature conditions compared to other parts. At the same time, due to the temperature decrease when passing through the pore, there is a greater stress difference compared with other parts of the rock along the direction of temperature transfer, so the heating of the pore in the rock is more likely to cause damage.

Analysis was conducted on the different positions and long-axis directions of a single pore. The pore at different positions was subjected to different temperatures, resulting in different pore stresses and damages in the rock. To study the mutual influence of different pores, temperature, stress, and damage analyses were performed on pores K1~K4 at different intervals and planes. Fig. (**6**) shows the mutual influence of parallel pores under different speeds. The location of the pore is divided into different planes. Fig. (**6a**) flashes the temperature, stress, and damage distribution of the heated rock with a heat source of V_4=20cm/s and R=7mm. When high temperature passes through the pore, it can be seen from the distribution of the z-plane that the temperature distribution of the rock with pores is wider, especially along the vertical direction of heating, and the longer the ellipse axis, the wider the temperature propagation. The different intervals between pores have little effect on the

temperature propagation. When comparing the y-plane, it is found that the pore can prevent the temperature from propagating downward. When the temperature propagates downward, the longer the ellipse axis and the closer the distance between the pores, the more significant the inhibitory effect. Similar to the temperature distribution, there is no obvious pattern in the stress distribution of the z-plane. It seems to be only affected by the rock material, and the stress shows the characteristics of a single pore. The distribution of the axis direction and the interval between pores do not affect the distribution of stress, and there is no obvious interaction between multiple pores. From the y-plane view, the distance between the pores has a certain impact on the stress distribution between the pores based on the distribution of stress of a single pore. The stress between the pores is inversely proportional to the distance between the pores and is unrelated to the direction of the long axis. Under this heating condition, when the heat transfer direction is perpendicular to the line connecting the two pores, the ratio of the half-axis length of the pore to the distance between pores is greater than or equal to 1, and the influence between pores can be ignored. From the perspective of the z-plane, the material distribution of the rock is the biggest factor affecting the damage of the rock and is unrelated to the distance between pores. The damage and stress in the y-plane correspond well, and the farther the distance between the pores, the smaller the damage of the rock.

As a comparison, the diagram distribution under the heating condition of V_2=10cm/s and R=7mm in Fig. (**6b**) is compared with Fig. (**6a**). When the heating source moves slowly, the heating time of the rock is prolonged, and the overall temperature, stress, and damage become more prominent, and the phenomenon is more significant, with higher temperatures, stress, and damage in the pores. Similar to the temperature distribution in Fig. (**6a**), due to the higher temperatures in the z-plane and y-plane of Fig. (**6b**), the temperature distribution and stress distribution of the pore locations can be seen, which also matches with Fig. (**6a**). As the temperature increases, the damage values and damage range gradually increase, with the damage diagram and temperature distribution in the z-plane corresponding to each other, while the depth of damage in the y-plane increases significantly. At this time, the damage range has covered the bottom of the pores parallel to the section α and z-plane. Pore damage extends downward along the two end points of the heat transfer path and is prone to occur at the pores' edges. At this time, the spacing between the pores can promote damage development well, and the closer the distance, the easier the pore edge is to be damaged. The relationship between rock pore distance and thermal damage is also related to the heating speed, and the higher the temperature, the greater the distance of the mutual influence of thermal damage between the pores.

4.2. Pore Damage

A comparison was made of the damage to rocks with and without pores under different heating rates to study the effect of pores on rock damage in Fig. (**7**). The results show that both curves exhibit a decrease in rock damage with increasing heating rates. It can be seen that, under the same heating conditions, rocks with pores suffer greater damage than those without pores, and the growth of the two curves follows an exponential function as the heating source moves slower. Rocks with pores have a faster growth rate, consistent with previous conclusions: the higher the temperature, the easier it is to generate damage near the edges of the pores. Therefore, from the perspective of damage distribution, the damage to rocks with pores is concentrated around the pore location, and the damage level at the center position is higher, while the damage distribution is more uniform without pores.

Brittle damage such as thermal spalling is the main type of rock thermal damage, and Fig. (**8**) unveils the damage patterns and comparison curves with and without pores. Rock thermal damage includes tensile damage and shear damage, where tensile damage accounts for a greater proportion of total damage, while shear damage only accounts for a small part and has a lower degree of damage, hardly affecting the total damage or tensile damage. From the perspective of damage distribution, shear damage exhibits distinct features, that is, shear damage mainly distributes in the middle position between pores and the heated surface, and the farther away from the heated surface, the lower the degree of shear damage. The closer the distance between multiple pores, the more significant the degree of shear damage, and this increasing trend is faster than that of shear damage without pores. As shear damage accounts for a small proportion, it can be considered that the changes in trend and distribution of tensile damage are consistent with those of total damage.
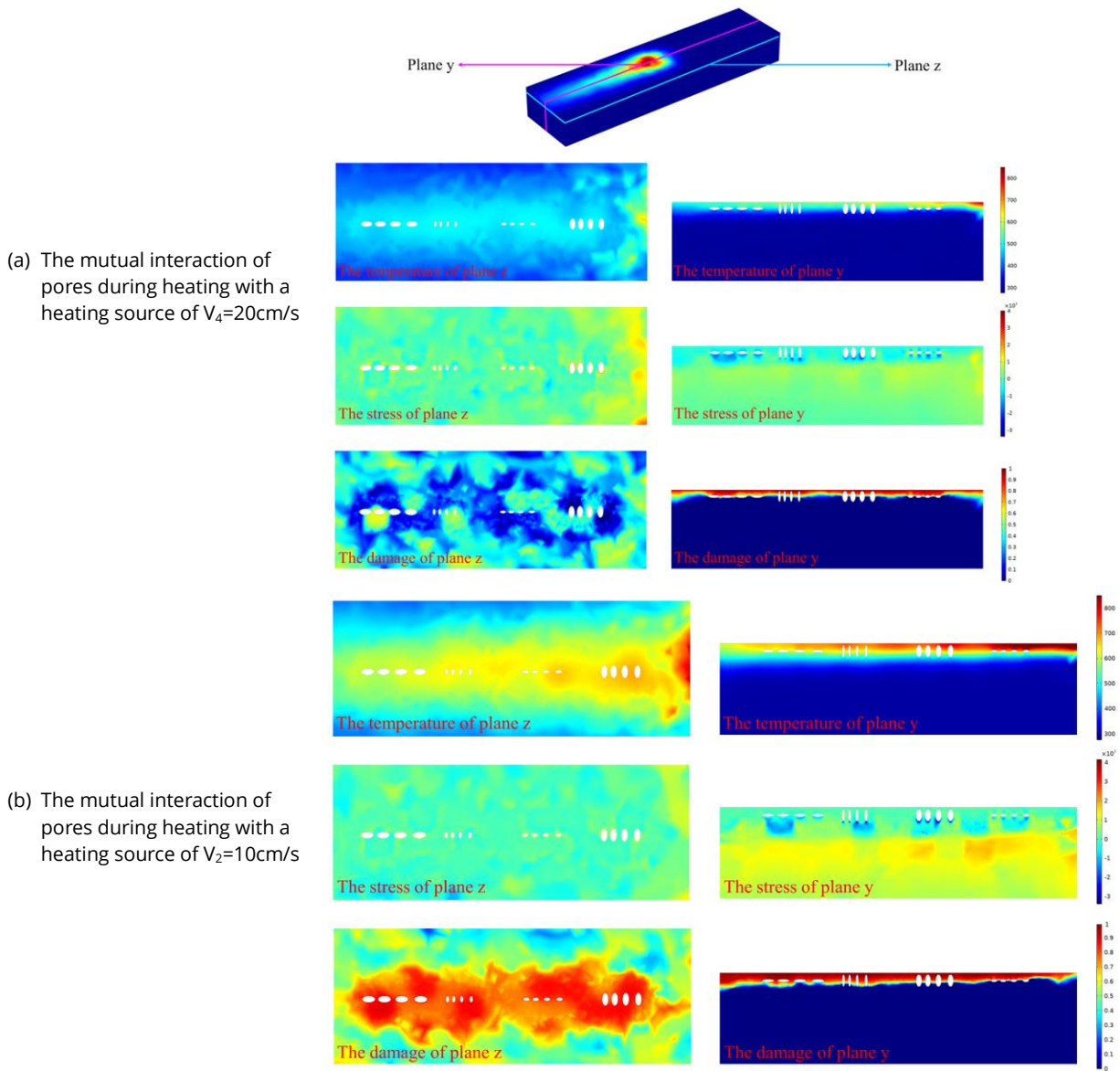
(a) The mutual interaction of pores during heating with a heating source of V_4=20cm/s

(b) The mutual interaction of pores during heating with a heating source of V_2=10cm/s

Figure 6: The mutual interaction between adjacent pores.
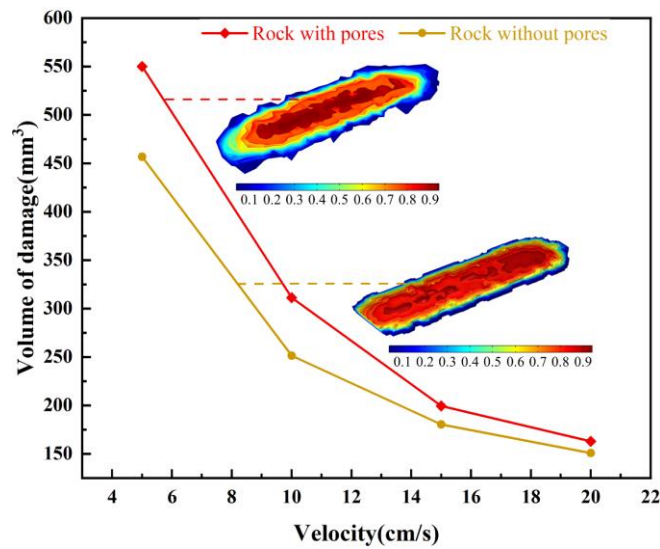

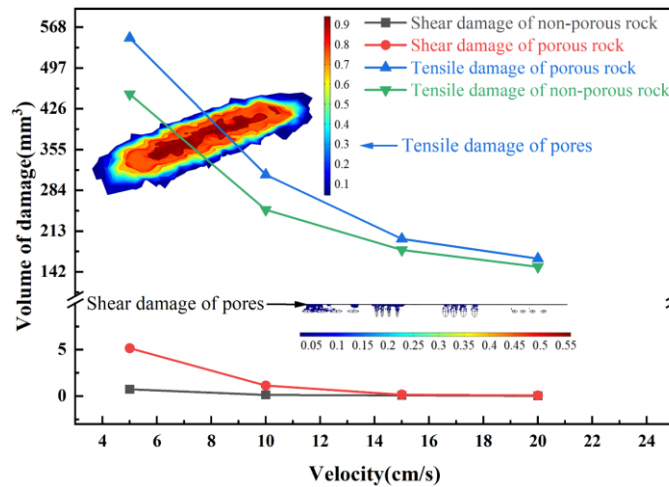**Figure 7:** Changes in rock damage with and without pores.

Figure 8: The comparison of damage patterns with and without pores.

To investigate the influence of pore size on the thermal damage of rocks, the K5-K9 pores were analyzed. Keeping the two semi-axis sizes constant, the long-axis size of the pores was changed. When the size was 0.1mm, the pore was spherical. Increasing the long axis size, the pore became longer, with a circular γ-section, and the α-section and β-section were both ellipses. Fig. (**9**) displays the distribution and variation of pore damage at different long-axis sizes. It can be seen that pore damage spreads from both ends of the long axis to the middle, with greater damage on the upper surface and smaller damage on the lower surface as the pore length increases. The pore length influences the damage distance. The overall damage increased with the long axis size of the pore, as indicated by the variation of the curve. The damage of the rock was still mainly tensile, accounting for more than 95%, and its damage growth curve was consistent with the trend of total damage, with similar values. Shear damage was a relatively smaller proportion and its variation was negligible during the entire heating process.
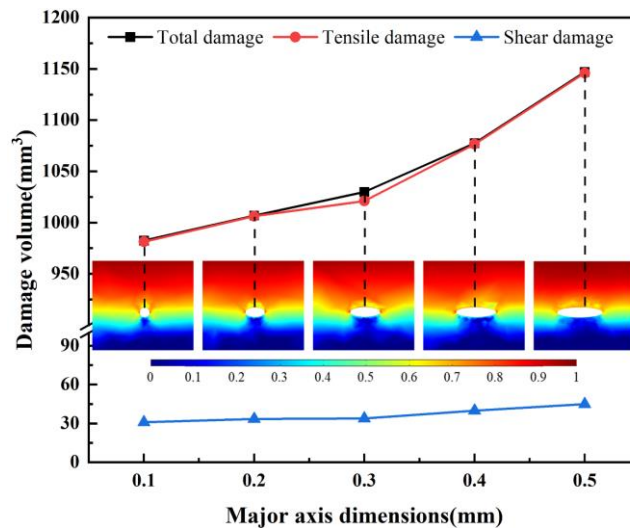

Figure 9: The influence of pore long axis size on rock damage.

Different pore distances have a significant impact on the thermal damage of rocks. In the analysis of pore distance, it was concluded that the distance between pores is inversely proportional to rock damage. To study the impact of different pore densities on rock damage, the K10-K13 pore models were simulated. Changing the pore density in the rock model can change the distance between pores and reveal the impact pattern in randomly distributed pores. Fig. (**10**) shows the effect of pore density on rock thermal damage. The proportions of total damage, tensile damage, and shear damage shown in the figure are consistent with the previous discussion. However, from the growth curve, it can be found that the different damage curves increase approximately proportionally with the increasing pore density of the rock.
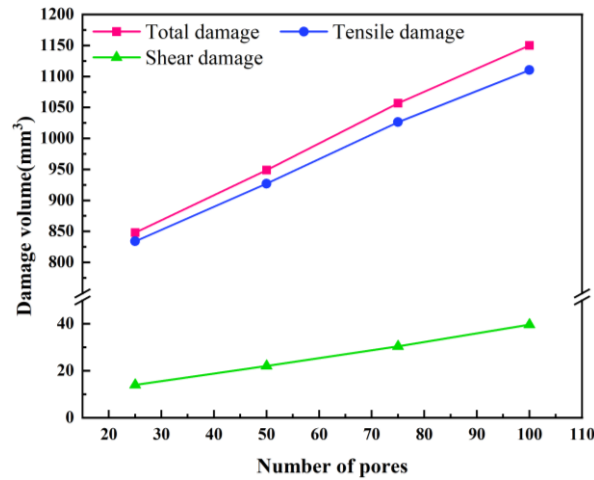
Figure 10: The impact of pore quantity on rock thermal damage.

As revealed in Fig. (**11**), the comparison of pore quantity and rock thermal damage distribution is presented. Among them, K10 to K13 pores increase in number, and the areas with higher damage are concentrated around the heating center. Rocks with fewer pores have lower and discontinuous damage and less damage. As the number of pores increases, the distance between the pores in the rock gradually decreases. When different pores are less than a certain distance, the mutual influence between pores will increase the stress and damage. Local rocks between pores are more likely to generate larger damage than other areas. Therefore, damage in rocks with more pores tends to have a more uniform damage distribution and higher degrees of damage.
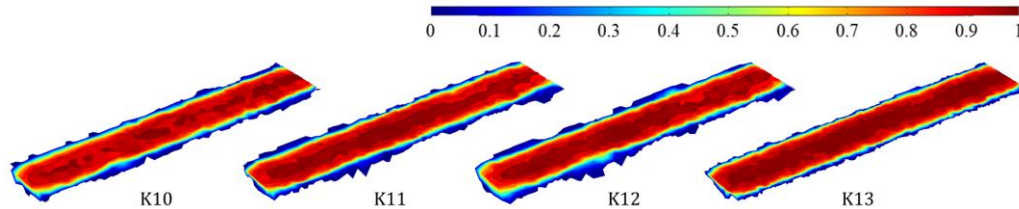

Figure 11: The distribution of thermal damage in rocks with different pore quantities.

In summary, the longer the long-axis size of rock pores and the more pores there are, the higher the degree of thermal damage in rocks and the more concentrated the damage is. Tensile damage dominates the type of rock damage, while shear damage mainly occurs at the edges of pores, which have a lower damage and degree of damage.

5. Conclusions

The thermo-mechanical coupling model of heterogeneous rocks was utilized to incorporate pores with varying angles, sizes, and positions. By analyzing the temperature, stress, and damage distribution of these pores under heating conditions, the thermal spalling damage mechanism was uncovered. The following conclusions are meaningful:

1. Locally heating heterogeneous porous rocks at high temperatures increases tensile damage and decreases shear damage, which mostly occurs at pores. However, as pores move and form, shear, and tensile damage ratios alter. In particular, shear damage increases as the pore approaches the heating surface, and tensile damage increases as it moves away

2. Rock pores diminish temperature along temperature transfer, increasing stress differences at the pore location. However, holes parallel to the heating surface increase temperature transmission. The stress distribution of pores is highly correlated with the isothermal surface. Higher pore curvature at the isothermal surface makes stress accumulation and damage simpler.

3. The slower the heat source, the longer the granite will heat up, increasing its pores, stress, and damage. The rock damage range will expand.

4. Longer pores mean shorter distances between pores, and higher pore density means more rock damage. The damage caused by rock heating the pores concentrates on the space between the pore and the heating surface, and the closer the distance, the greater the effect.

The present research examines how pore length and density affect thermal fracture damage during thermally assisted rock cutting. The findings provide a theoretical framework for understanding how pore structure impacts thermal spalling in deep oil and gas reservoirs. Pore exploration-based rock fracture research may be added in the future, creating the theoretical framework for this technology.

Conflict of Interest

The authors confirm that this article's content has no conflict of interest.

Funding

References

[1]   Guo X, Hu D, Li Y, Duan J, Zhang X, Fan X, *et al*. Theoretical progress and key technologies of onshore ultra-deep oil/gas exploration. Engineering. 2019; 5: 458-70. https://doi.org/10.1016/j.eng.2019.01.012

[2]   Wu N-H, Gao M-Z, Zhu L-Y, Li J-N, Fan D, You B, *et al*. Pressure control method and device innovative design for deep oil in-situ exploration and coring. Pet Sci. 2022; 20: 1169-82. https://doi.org/10.1016/j.petsci.2022.10.011

[3]   Li J, Zhang Z, Zhu G, Li T, Zhao K, Chi L, *et al*. The origin and accumulation of ultra-deep oil in Halahatang area, northern tarim basin. J Pet Sci Eng. 2020; 195: 107898. https://doi.org/10.1016/j.petrol.2020.107898

[4]   Cheng B, Liu H, Cao Z, Wu X, Chen Z. Origin of deep oil accumulations in carbonate reservoirs within the north Tarim Basin: Insights from molecular and isotopic compositions. Org Geochem. 2020; 139: 103931. https://doi.org/10.1016/j.orggeochem.2019.103931

[5]   Fang T, Li S, Zhang Y, Su Y, Yan Y, Zhang J. How the oil recovery in deep oil reservoirs is affected by injected gas types: A molecular dynamics simulation study. Chem Eng Sci. 2021; 231: 116286. https://doi.org/10.1016/j.ces.2020.116286

[6]   Lei Q, Xu Y, Yang Z, Cai B, Wang X, Zhou L, *et al*. Progress and development directions of stimulation techniques for ultra-deep oil and gas reservoirs. Pet Explor Dev. 2021; 48: 221-31. https://doi.org/10.1016/S1876-3804(21)60018-6

[7]   Qi Y, Cai C-F, Sun P, Wang D-W, Zhu H-J. Crude oil cracking in deep reservoirs: A review of the controlling factors and estimation methods. Pet Sci. 2023; 20: 1978-97. https://doi.org/10.1016/j.petsci.2023.03.006

[8]   Imran QS, Ahmad Siddiqui N, Abdul Latif AH, Bashir Y, Abduh Saeed Ali AA, Jamil M. Integrated well data and 3D seismic inversion study for reservoir delineation and description. Bull Geol Soc Malaysia. 2020; 70: 209-20. https://doi.org/10.7186/bgsm70202016

[9]   Bashir Y, Faisal MA, Biswas A, Babasafari A abbas, Ali SH, Imran QS, *et al*. Seismic expression of miocene carbonate platform and reservoir characterization through geophysical approach: application in central Luconia, offshore Malaysia. J Pet Explor Prod. 2021; 11: 1533-44. https://doi.org/10.1007/s13202-021-01132-2

[10]   Huang Y, Kong Y, Cheng Y, Zhu C, Zhang J, Wang J. Experimental study on inversion of micro-pore structure of buried hill reservoir in Bohai sea. Geothermics. 2023; 107: 102584. https://doi.org/10.1016/j.geothermics.2022.102584

[11]   Rossi E, Kant MA, Madonna C, Saar MO, Rudolf von Rohr P. The effects of high heating rate and high temperature on the rock strength: Feasibility study of a thermally assisted drilling method. Rock Mech Rock Eng. 2018; 51: 2957-64. https://doi.org/10.1007/s00603-018-1507-0

[12]   Wu F, Zhang D, Ma L, Meng T, Zhao G, Liu P, *et al*. Thermo-hydro-mechanical (THM) evolution law and development of permeability and pore structure of enhanced geothermal systems at ultra-high temperatures. Geothermics. 2021; 97: 102253. https://doi.org/10.1016/j.geothermics.2021.102253

[13]   Gao M, Zhang K, Zhou Q, Zhou H, Liu B, Zheng G. Numerical investigations on the effect of ultra-high cutting speed on the cutting heat and rock-breaking performance of a single cutter. J Pet Sci Eng. 2020; 190: 107120. https://doi.org/10.1016/j.petrol.2020.107120

[14]   Wang H, Liao H, Niu W, Xu J, Liu Y, He Y. Enhancing rock drilling efficiency: Evaluating the effectiveness of ultra-high-pressure water jet slotting technology in granite drilling. Geoenergy Sci Eng. 2023; 228: 212075. https://doi.org/10.1016/j.geoen.2023.212075

[15]   Valley B, Evans KF. Stress orientation to 5 km depth in the basement below Basel (Switzerland) from borehole failure analysis. Swiss J Geosci. 2009; 102: 467-80. https://doi.org/10.1007/s00015-009-1335-z

[16]   Busahmin B, Saeid NH, Alusta G, Zahran ESMM. Review on hole cleaning for horizontal wells. ARPN J Eng Appl Sci. 2017; 12: 4697-708.

[17]   Augustine C, Tester JW. Hydrothermal flames: From phenomenological experimental demonstrations to quantitative understanding. J Supercrit Fluids. 2009; 47: 415-30. https://doi.org/10.1016/j.supflu.2008.10.003

[18]   Rossi E, Jamali S, Saar MO, Rudolf von Rohr P. Field test of a combined thermo-mechanical drilling technology. Mode I: Thermal spallation drilling. J Pet Sci Eng. 2020; 190: 107005. https://doi.org/10.1016/j.petrol.2020.107005

[19]   Höser D, Meier T, Patru A, Kant M, Rudolf von Rohr Ph. An experimental study of the influence of uniaxial load on flame jet drilling. Int J Rock Mech Min Sci. 2018; 106: 311-8. https://doi.org/10.1016/j.ijrmms.2018.04.007

[20]   Rossi E, Jamali S, Schwarz D, Saar MO, Rudolf von Rohr P. Field test of a Combined Thermo-Mechanical Drilling technology. Mode II: Flame-assisted rotary drilling. J Pet Sci Eng. 2020; 190: 107005. https://doi.org/10.1016/j.petrol.2019.106880

[21]   Rong G, Peng J, Yao M, Jiang Q, Wong LNY. Effects of specimen size and thermal-damage on physical and mechanical behavior of a fine-grained marble. Eng Geol. 2018; 232: 46-55. https://doi.org/10.1016/j.enggeo.2017.11.011

[22]   Kumari WGP, Ranjith PG, Perera MSA, Chen BK, Abdulagatov IM. Temperature-dependent mechanical behaviour of australian strathbogie granite with different cooling treatments. Eng Geol. 2017; 229: 31-44. https://doi.org/10.1016/j.enggeo.2017.09.012

[23]   Yang Y, Zhuang D, Ding G, Hu H. Observation and description of the shape of water bridge retaining between vertical plane surfaces. Int J Refrig. 2016; 64: 20-31. https://doi.org/10.1016/j.ijrefrig.2016.01.009

[24]   Lai J, Wang G, Wang Z, Chen J, Pang X, Wang S, *et al*. A review on pore structure characterization in tight sandstones. Earth-Science Rev. 2018; 177: 436-57. https://doi.org/10.1016/j.earscirev.2017.12.003

[25]   Pan J, Zhang Z, Li M, Wu Y, Wang K. Characteristics of multi-scale pore structure of coal and its influence on permeability. Nat Gas Ind B. 2019; 6: 357-65. https://doi.org/10.1016/j.ngib.2019.01.012

[26]   Xu Y, Lun Z, Pan Z, Wang H, Zhou X, Zhao C, *et al*. Occurrence space and state of shale oil: A review. J Pet Sci Eng. 2022; 211: 110183. https://doi.org/10.1016/j.petrol.2022.110183

[27]   Liu Q, Sun M, Sun X, Liu B, Ostadhassan M, Huang W, *et al*. Pore network characterization of shale reservoirs through state-of-the-art X-ray computed tomography: A review. Gas Sci Eng. 2023; 113: 204967. https://doi.org/10.1016/j.jgsce.2023.204967

[28]   Wu Y, Tahmasebi P, Lin C, Zahid MA, Dong C, Golab AN, *et al*. A comprehensive study on geometric, topological and fractal characterizations of pore systems in low-permeability reservoirs based on SEM, MICP, NMR, and X-ray CT experiments. Mar Pet Geol. 2019; 103: 12-28. https://doi.org/10.1016/j.marpetgeo.2019.02.003

[29]   Xu Z, Lin M, Jiang W, Cao G, Yi Z. Identifying the comprehensive pore structure characteristics of a rock from 3D images. J Pet Sci Eng. 2020; 187: 106764. https://doi.org/10.1016/j.petrol.2019.106764

[30]   Wu Y, Tahmasebi P, Lin C, Zahid MA, Dong C, Golab AN, *et al*. A comprehensive study on geometric, topological and fractal characterizations of pore systems in low-permeability reservoirs based on SEM, MICP, NMR, and X-ray CT experiments. Mar Pet Geol. 2019; 103: 12-28. https://doi.org/10.1016/j.marpetgeo.2019.02.003

[31]   Cid HE, Carrasco-Núñez G, Manea VC. Improved method for effective rock microporosity estimation using X-ray microtomography. Micron. 2017; 97: 11-21. https://doi.org/10.1016/j.micron.2017.01.003

[32]   Ju Y, Yang Y, Song Z, Xu W. A statistical model for porous structure of rocks. Sci China, Ser E Technol Sci. 2008; 51: 2040-58. https://doi.org/10.1007/s11431-008-0111-z

[33]   Shang X, Zhang Z, Xu X, Liu T, Xing Y. Mineral composition, pore structure, and mechanical characteristics of pyroxene granite exposed to heat treatments. Minerals. 2019; 9(9): 553. https://doi.org/10.3390/min9090553

[34]   Zhao Y, Meng Q, Kang T, Zhang N, Xi B. Micro-CT experimental technology and meso-investigation on thermal fracturing characteristics of granite. Chinese J Rock Mech Eng. 2008; 27: 28-34.

[35]   Zhang Z, Gao F, Gao Y, Xu X, Hou P, Teng T, *et al*. Fractal structure and model of pore size distribution of granite under high temperatures. Yanshilixue Yu Gongcheng Xuebao/Chinese J Rock Mech Eng. 2016; 35: 2426-38. https://doi.org/10.13722/j.cnki.jrme.2016.0798

[36]   Chaki S, Takarli M, Agbodjan WP. Influence of thermal damage on physical properties of a granite rock: Porosity, permeability and ultrasonic wave evolutions. Constr Build Mater. 2008; 22: 1456-61. https://doi.org/10.1016/j.conbuildmat.2007.04.002

[37]   Wu X, Cai M, Zhu Y, Guo Q, Wang P, Dong J. Case Studies in Thermal Engineering An experimental study on the fractal characteristics of the effective pore structure in granite by thermal treatment. Case Stud Therm Eng. 2023; 45: 102921. https://doi.org/10.1016/j.csite.2023.102921

[38]   Zhao ZL, Jing HW, Wu JY, Shi XS, Gao Y, Yin Q. Experimental investigation on damage characteristics and fracture behaviors of granite after high temperature exposure under different strain rates. Theor Appl Fract Mech. 2020; 110: 102823. https://doi.org/10.1016/j.tafmec.2020.102823

[39]   Cao R, Fang L, Qiu X, Lin H, Li X, Li W, *et al*. Effect of heating–water cooling cycle treatment on the pore structure and shear fracture characteristics of granite. Eng Fract Mech. 2023; 286: 109263. https://doi.org/10.1016/j.engfracmech.2023.109263

[40]   Hao J, Qiao L, Li Q. Study on cross-scale pores fractal characteristics of granite after high temperature and rock failure precursor under uniaxial compression. Powder Technol. 2022; 401: 117330. https://doi.org/10.1016/j.powtec.2022.117330

[41]   Yang S, Li X, Zhang K, Yu Q, Du X. The coupling effects of pore structure and rock mineralogy on the pre-Darcy behaviors in tight sandstone and shale. J Pet Sci Eng. 2022; 218: 110945. https://doi.org/10.1016/j.petrol.2022.110945

[42]   YunJiang C, PeiChun W, ShengQing L, WenHao W, Lei X, HeMing W. Experimental study on inversion of micro-pore structure of buried hill reservoir in Bohai Sea. Prog Geophys 2022; 38(4): 1757-64. https://doi.org/10.6038/pg2023GG0373

[43]   Alashloo SYM, Bashir Y, Ghosh DP. Anisotropic modeling and imaging. In: Seism Imaging Methods and Applications for Oil and Gas Exploration, Elsevier; 2022, p. 133-78. https://doi.org/10.1016/B978-0-323-91946-3.00001-8

[44]   Jiang HP, Jiang AN, Yang XR. Statistical damage constitutive model of high temperature rock based on Weibull distribution and its verification. Rock Soil Mech. 2021; 42: 1894-902. https://doi.org/10.16285/j.rsm.2020.1461

[45]   Wang ZL, Shi H, Wang JG. Mechanical behavior and damage constitutive model of granite under coupling of temperature and dynamic loading. Rock Mech Rock Eng. 2018; 51: 3045-59. https://doi.org/10.1007/s00603-018-1523-0

[46]   Zhu WC, Liu J, Yang TH, Sheng JC, Elsworth D. Effects of local rock heterogeneities on the hydromechanics of fractured rocks using a digital-image-based technique. Int J Rock Mech Min Sci. 2006; 43: 1182-99. https://doi.org/10.1016/j.ijrmms.2006.03.009

[47]   Zhu WC, Wei CH, Tian J, Yang TH, Tang CA. Coupled thermal-hydraulic-mechanical model during rock damage and its preliminary application. Rock Soil Mech. 2009; 30 (12): 3851-7.

[48]   Zhou Y, Rajapakse R, Graham J. A coupled thermoporoelastic model with thermo-osmosis and thermal-filtration. Int J Solids Struct. 1998; 35: 4659-83. https://doi.org/10.1016/S0020-7683(98)00089-4

[49]   Tiankui G, Songjun T, Shun L, Xiaoqiang L, Wei Z, Guanzheng Q. Numerical simulation of hydraulic fracturing of hot dry rock under thermal stress. Eng Fract Mech. 2020: 240: 107350. https://doi.org/10.1016/j.engfracmech.2020.107350

[50]   Wancheng Z, Chenhui W, Fuzhuang Z, Tianhong Y. Investigation of water inrush from karst subsidence column by using a coupled hydramechanical model. Chin J Undergr Space Eng. 2009; 5: 928-33.

[51]   Zhu WC, Wei CH, Liu J, Qu HY, Elsworth D. A model of coal–gas interaction under variable temperatures. Int J Coal Geol J. 2011; 86: 213-21. https://doi.org/10.1016/j.coal.2011.01.011

[52]   Peng J, Wong LNY, Teh CI. Influence of grain size heterogeneity on strength and microcracking behavior of crystalline rocks. J Geophys Res Solid Earth Res. 2017; 122: 1054-73. https://doi.org/10.1002/2016JB013469

[53]   Weiji L, Feilong Y, Hongduo D, Run C, Xiaohua Z. Investigate on the mixed-cutting of Specially-shaped PDC cutters in granite. Eng Mech. 2023; 40: 245-56.

[54]   Zhu X, Luo Y, Liu W, Hu H, Chen M. Numerical electric breakdown model of heterogeneous granite for electro-pulse-boring. Int J Rock Mech Min Sci. 2022; 154: 105128. https://doi.org/10.1016/j.ijrmms.2022.105128